

Low-Energy Effective Hamiltonian and the Surface States of Ca_3PbO

Toshikaze KARIYADO* and Masao OGATA

Department of Physics, the University of Tokyo, Bunkyo, Tokyo 113-0033, Japan

The band structure of Ca_3PbO , which possesses a three-dimensional massive Dirac electron at the Fermi energy, is investigated in detail. Analysis of the orbital weight distributions on the bands obtained in the first-principles calculation reveals that the bands crossing the Fermi energy originate from the three Pb- p orbitals and three Ca- $d_{x^2-y^2}$ orbitals. Taking these Pb- p and Ca- $d_{x^2-y^2}$ orbitals as basis wave functions, a tight-binding model is constructed. With the appropriate choice of the hopping integrals and the strength of the spin-orbit coupling, the constructed model successfully captures important features of the band structure around the Fermi energy obtained in the first-principles calculation. By applying the suitable basis transformation and expanding the matrix elements in the series of the momentum measured from a Dirac point, the low-energy effective Hamiltonian of this model is explicitly derived and proved to be a Dirac Hamiltonian. The origin of the mass term is also discussed. It is shown that the spin-orbit coupling and the orbitals other than Pb- p and Ca- $d_{x^2-y^2}$ orbitals play important roles in making the mass term finite. Finally, the surface band structures of Ca_3PbO for several types of surfaces are investigated using the constructed tight-binding model. We find that there appear nontrivial surface states that cannot be explained as the bulk bands projected on the surface Brillouin zone. The relation to the topological insulator is also discussed.

KEYWORDS: Dirac electron, inverse perovskite, Ca_3PbO , the first-principles calculation, tight-binding model

1. Introduction

A low-energy effective Hamiltonian of a material sometimes becomes a relativistic Dirac Hamiltonian despite the fact that electrons in materials are basically described by a nonrelativistic Hamiltonian and the perturbative treatment of the relativistic effects is generally legitimated. Such an emergent “Dirac electron” is known to host many intriguing phenomena. The well-known and well studied realizations of the emergent Dirac electrons in materials are graphene^{1–3} (two-dimensional, massless) and bismuth⁴ (three-dimensional, massive). It is also known that an organic compound, α -(BEDT-TTF)₂I₃, has Dirac electrons in the band structure near the Fermi energy.^{5,6} Rather new example of emergent Dirac electrons are surface states of three-dimensional topological insulators,⁷ which attract great interests and are extensively studied in these days. Another new example is SrMnBi₂, which is claimed to have a two-dimensional strongly-anisotropic massive Dirac electron.^{8–10} A Weyl fermion, which has a linear dispersion but is described by 2×2 (not 4×4) matrix is also claimed to exist in Y₂Ir₂O₇,¹¹ where the time reversal symmetry is broken by a magnetic order.

Recently, we proposed an inverse-perovskite material Ca_3PbO and its family as candidates for new materials having Dirac electrons. The first-principles calculation shows that a three-dimensional massive Dirac electron appears in the low-energy band structure of Ca_3PbO .¹² A Dirac point, which is defined as the center of linear dispersion of the Dirac electron, is located on the Γ -X line. Due to the cubic symmetry of this material, existence of a Dirac point on the Γ -X line implies that there are six equivalent Dirac points in the Brillouin zone. The

most remarkable feature of the Dirac electron in Ca_3PbO is that it appears exactly at the Fermi energy, and the bands forming the Dirac electron are the only bands that cross the Fermi energy. Namely, the Dirac type linear dispersion is the only feature comes up in the vicinity of the Fermi energy.

This point gives a strong contrast to bismuth, which is a well-known and well studied example having three-dimensional massive Dirac electron in its band structure. In bismuth, not only bands with Dirac type linear dispersion, but also a band with parabolic dispersion intersects the Fermi energy and gives a usual hole Fermi surface.^{13,14} As a result, one has to dope some carriers in order to investigate the properties related to the Dirac electrons.¹⁵ With this respect, it is important to study Ca_3PbO , which has a simpler band structure than bismuth, in order to obtain a deeper understanding of three-dimensional Dirac electrons in materials. Furthermore, high symmetry of the crystal structure of Ca_3PbO enables us to have an intuitive view on the origin of Dirac electron in Ca_3PbO by analyzing the symmetry of wave functions for the states relevant to the Dirac electron.¹² The main topic of this paper is to show the details of such an analysis that was briefly reported before.¹² The origin of Dirac electron in bismuth is complicated^{16,17} and its simple and intuitive picture is still missing. Therefore, the analysis of Ca_3PbO demonstrated in the following will also give hints for the case of bismuth.

In this paper, a detailed analysis of the band structure of Ca_3PbO is presented. First, we construct a tight-binding model that captures important features of the band structure near the Fermi energy obtained in the first-principles calculation. It is assigned that the three Pb- p orbitals and three Ca- $d_{x^2-y^2}$ orbitals [Fig. 3(b)] should be included in the tight-binding model by an

*E-mail address: kariyado@hosi.phys.s.u-tokyo.ac.jp

alyzing the orbital weight distributions on the bands. With the proper choice of the hopping parameters and the strength of the spin-orbit coupling, the band structure obtained in the first-principles calculation is fairly well reproduced by the constructed simple tight-binding model. The analysis is farther proceeded and we prove that the low-energy effective Hamiltonian is really a Dirac Hamiltonian by applying a proper basis transformation and by expanding the matrix elements with respect to the momentum measured from one of the Dirac points. It is worth noting that not only the Hamiltonian, but also the basis wave functions of the low-energy effective model are explicitly obtained. These basis wave functions play a role of pseudospins of the Dirac model. We will also discuss the mass term of the Dirac Hamiltonian in this material, which has been only briefly mentioned in our previous paper.¹² Especially, the roles of the spin-orbit coupling and the orbitals other than Pb- p and Ca- $d_{x^2-y^2}$ orbitals are explained. The relation between Ca_3PbO and a topological insulator is also discussed. It is shown that Ca_3PbO is not a topological insulator. Finally, the surface band structures of Ca_3PbO are studied using the constructed tight-binding model. It is found that there exist nontrivial surface bands that are nondegenerate and are not explained as the bulk states projected on the surface Brillouin zone.

This paper is organized as follows. Section 2 is used to describe details of the method for calculation. In §3, the orbital weight distributions on the obtained bands are analyzed and a tight-binding model is constructed. Section 4 is devoted for analyzing the obtained tight-binding model and proving that its low-energy part is actually described by a Dirac Hamiltonian. At the end of §4, the origin of the mass term is also discussed. In §5, we make arguments on the topological properties and the surface band structures. The paper is summarized in §6.

2. First-Principles Calculation

The band structure calculation is carried out using WIEN2k package,¹⁸ in which the full-potential augmented-plane-wave method is implemented. The crystal parameters required in the calculation are taken from the experimental results.¹⁹ Figure 1 shows the crystal structure of Ca_3PbO . Perdew-Burke-Ernzerhof generalized-gradient approximation²⁰ is used for the exchange-correlation functional. The parameter choice of $(RK_{\text{max}}, G_{\text{max}}) = (9.0, 14.0)$ is used, while radii of spherical atomic region for Ca, Pb, and O are chosen to be 2.28, 2.50, and 2.28 (a.u.), respectively. 220 momentum points in the irreducible Brillouin zone, which are reduced from $20 \times 20 \times 20$ momentum points in the full Brillouin zone, are employed in the self-consistent cycle in the present calculation. A spin-orbit coupling is taken into account within the spherical atomic region of each atom via second variational step.²¹

We have verified that changes in the parameters stated above (RK_{max} , G_{max} , radii of spherical atomic region, and the number of momentum points) do not modify the results in this paper, e.g., appearance of the Dirac type dispersion in the vicinity of Fermi energy. Although the experimental crystal parameters are used in the cal-

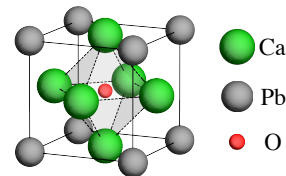


Fig. 1. (Color online) Crystal structure of Ca_3PbO .

ulation, it should be noted that the previous theoretical works showed that the optimized lattice constants for Ca_3PbO and its family obtained in the first-principles calculation agree well with the experimental data,^{22,23} indicating the consistency between theory and experiments.

A special care should be paid in the treatment of the spin-orbit coupling. Namely, we should be careful in applying the second variational step to heavy elements such as Pb in which the spin-orbit coupling is expected to be strong.²¹ However, we think that this is not a serious problem in our calculation. One of the reasons is that only the state with the total angular momentum $J = 3/2$ is important for the Dirac electron in this material as will be explained later, while the second variational step mainly causes problems for $J = 1/2$ state.²¹ Another reason is that the band structure does not change (except for unimportant points) even if we use the pseudopotential method²⁴ with fully-relativistic pseudopotential for Pb atom in which the spin-orbit coupling is treated better than in the second-variational step.

3. Construction of the Tight-Binding Model

3.1 Orbital Character of Each Band

The obtained band structure of Ca_3PbO is presented in Fig. 2 together with the orbital weight distributions for Ca $d_{3z^2-r^2}$, d_{xy} , $d_{x^2-y^2}$, $d_{zx/yz}$, and Pb p orbitals. As is shown in ref. 12, there appears a Dirac electron on the Γ -X line, and the Dirac point is marked by an arrow in Fig. 2(a). The appearance of a Dirac point on the Γ -X line implies that there are six Dirac points in the whole Brillouin zone due to the cubic symmetry of this material. In other words, Dirac points are found at $(k_0, 0, 0)$, $(-k_0, 0, 0)$, $(0, k_0, 0)$, $(0, -k_0, 0)$, $(0, 0, k_0)$, and $(0, 0, -k_0)$. Although it is difficult to see in the presented energy scale, there exists a very small gap at the Fermi energy, and the emerged Dirac electron is actually massive with a very small mass. The magnitude of the mass gap is about 15 meV.¹²

Before moving on to the discussion on the orbital weight distributions, we explain the symmetry of the local environment of each atom. The local environment of the Ca atom has a tetragonal symmetry with its tetragonal axis directing along a line connecting the Ca and O atoms (see Fig. 1). The tetragonal-axis directions of the three Ca sites in the unit cell are different from each other. Then, it is convenient to introduce local coordinates for each Ca atom, whose definitions are illustrated in Fig. 3(a). Using these local coordinates, the Ca-3d orbitals can be classified into four groups, i.e., $d_{3z^2-r^2}$, d_{xy} ,

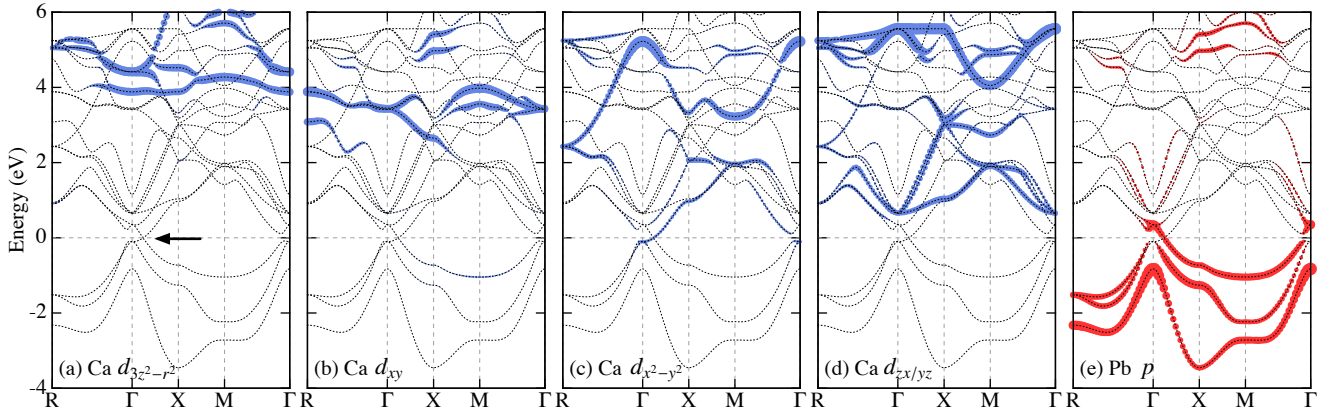


Fig. 2. (Color online) Orbital-weight distributions on the bands obtained in the first-principles calculation. (a)–(e) show the distribution of the Ca $d_{3z^2-r^2}$, Ca d_{xy} , Ca $d_{x^2-y^2}$, Ca $d_{zx/yz}$, and Pb p orbital weights, respectively. The orbital weights are represented as the width of the corresponding bands.

$d_{x^2-y^2}$, and $d_{zx/yz}$, reflecting the local tetragonal symmetry. Note that x , y , and z appearing in the subscripts refer to the local coordinates. On the other hand, the local environment of the Pb atom has a cubic symmetry and all Pb-6p orbitals (p_x , p_y , and p_z) are classified into a single group named as Pb- p .

The orbital weight distributions of Ca- $d_{3z^2-r^2}$, d_{xy} , $d_{x^2-y^2}$, and $d_{zx/yz}$ orbitals and Pb- p orbitals are plotted in Figs. 2(a)–2(e), where the weights are indicated by the width of each band. We can see that in the presented energy range, the bands below the Fermi energy mainly originate from Pb- p orbitals, while the highly entangled bands above the Fermi energy mainly originate from Ca-3d orbitals. However, note that the top of p-bands (bands originate from Pb-6p orbitals) locates above the bottom of d-bands (bands originate from Ca-3d orbitals) [Figs. 2(c) and 2(e)]. As will be discussed later, this overlap between the p- and d-bands is essential for the emergence of Dirac electron. Among the Ca-3d orbitals, the “center of mass” of Ca- $d_{3z^2-r^2}$ orbital weights lies at relatively high energy while that of Ca- $d_{x^2-y^2}$ lies at relatively low energy. This tendency can be understood from the crystal field splitting. Specifically, the orbitals whose lobes are directed to O or Pb (like Ca- $d_{3z^2-r^2}$) tend to have higher energy than the other orbitals since O and Pb are negatively charged in this material. On the other hand, the orbitals whose lobes are directed to direction other than O or Pb (like Ca- $d_{x^2-y^2}$) tend to have low energy. Note that Ca- $d_{x^2-y^2}$ and Ca- $d_{zx/yz}$ orbitals have large dispersion and their band widths exceed the energy difference of the center of masses of each orbital.

The most important information obtained from Figs. 2(a)–2(e) is that two bands forming the Dirac electron near the Fermi energy come from Ca- $d_{x^2-y^2}$ and Pb- p orbitals [see Figs. 2(c) and 2(e)]. For Ca- $d_{x^2-y^2}$ orbital, there are two reasons for this orbital to come down to the Fermi energy: one is its large dispersion and the other is that its center of mass lies at relatively low energy. On the basis of this observation, we neglect other Ca- d orbitals ($d_{3z^2-r^2}$, d_{xy} , and $d_{zx/yz}$) in constructing a model describing the Dirac electron in this material.

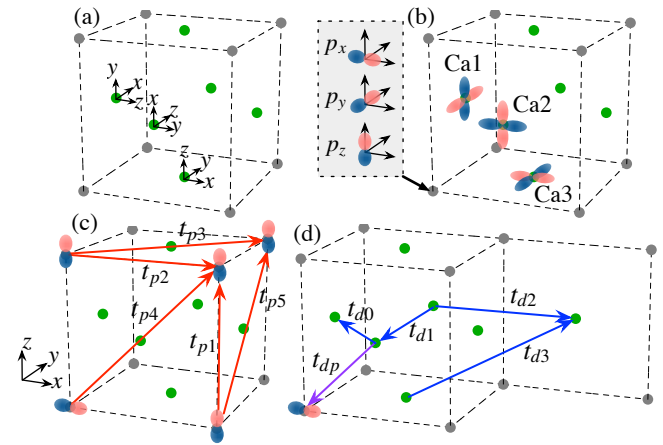


Fig. 3. (Color online) (a) The local coordinates on the three Ca sites in a unit cell. (b) Schematic pictures of the basis wave functions used in the reduced tight-binding model. (c,d) Definitions of hopping integrals between the two p -orbitals (c), between the two d -orbitals and between the p - and d -orbitals (d).

3.2 Tight-Binding Model

Now, we construct a tight-binding model that describes the low-energy band structure of Ca_3PbO . Based on the observations in the previous subsection, six orbitals, namely, three Pb- p orbitals (p_x , p_y , and p_z) and three Ca- $d_{x^2-y^2}$ orbitals in the unit cell are taken as basis orbitals. The three Ca- $d_{x^2-y^2}$ orbitals locate on Ca1, Ca2, and Ca3 site, respectively. See Figs. 1 and 3(b) for the definitions of Ca1, Ca2, and Ca3 sites and the schematic pictures for the basis orbitals. Note that x , y , and z appearing in the subscripts refer to the local coordinates as in Figs. 3(a) and 3(b). Furthermore, due to the strong spin-orbit coupling on the Pb atom, the spin degrees of freedom should be explicitly treated. As a result, we use 12 ($= 6 \times 2$) orbitals

$$|p_x \uparrow\rangle, |p_y \uparrow\rangle, |p_z \uparrow\rangle, |p_x \downarrow\rangle, |p_y \downarrow\rangle, |p_z \downarrow\rangle, \quad (1a)$$

$$|d_1 \uparrow\rangle, |d_2 \uparrow\rangle, |d_3 \uparrow\rangle, |d_1 \downarrow\rangle, |d_2 \downarrow\rangle, |d_3 \downarrow\rangle. \quad (1b)$$

Using these local orbitals as the basis set, we construct

a tight-binding Hamiltonian that is written as

$$\hat{H} = \sum_{\sigma} \sum_{\mathbf{r}\mathbf{a}\mathbf{r}'\mathbf{a}'} t_{aa'}(\mathbf{r} - \mathbf{r}') c_{\mathbf{r}\mathbf{a}\sigma}^{\dagger} c_{\mathbf{r}'\mathbf{a}'\sigma} + \sum_{\mathbf{r}\mathbf{a}\sigma\mathbf{r}'\mathbf{a}'\sigma'} \lambda_{aa'}^{\sigma\sigma'}(\mathbf{r} - \mathbf{r}') c_{\mathbf{r}\mathbf{a}\sigma}^{\dagger} c_{\mathbf{r}'\mathbf{a}'\sigma'} \quad (2)$$

where the indices a and a' represent $p_{x,y,z}$ or $d_{1,2,3}$, respectively. Hopping processes described in Figs. 3(c) and 3(d) are included in the first term of eq. (2) (details are explained soon later). The second term represents the spin-orbit coupling, which is assumed here to act only on the Pb- p orbitals for simplicity. The spin-orbit coupling on the Ca- d orbitals is neglected. The Fourier transformation of eq. (2) gives

$$\hat{H} = \sum_{\mathbf{k}} \sum_{\alpha\alpha'} \mathcal{E}_{\alpha\alpha'}(\mathbf{k}) c_{\mathbf{k}\alpha}^{\dagger} c_{\mathbf{k}\alpha'}, \quad (3)$$

where the indices α and α' run through 1 to 12, corresponding to the 12 basis orbitals in the order written in eqs. (1a) and (1b). As has been carried out in ref. 12, the matrix elements are transformed by attaching momentum-dependent phase factors to the basis orbitals as $|p_{x,y,z}\sigma\rangle \rightarrow e^{i(k_x+k_y+k_z)/2}|p_{x,y,z}\sigma\rangle$, $|d_1\sigma\rangle \rightarrow e^{ik_x/2}|d_1\sigma\rangle$, $|d_2\sigma\rangle \rightarrow e^{ik_y/2}|d_2\sigma\rangle$, and $|d_3\sigma\rangle \rightarrow e^{ik_z/2}|d_3\sigma\rangle$. This is performed for the matrix elements to have simple forms. The transformed basis and matrix elements are used hereafter.

Now, the Hamiltonian can be written in a compact form as

$$\hat{\mathcal{E}}_{\mathbf{k}} = \begin{pmatrix} \hat{\mathcal{E}}_{\mathbf{k}}^{pp} + \hat{\lambda}_{\mathbf{k}} & \hat{\mathcal{E}}_{\mathbf{k}}^{pd} \\ (\hat{\mathcal{E}}_{\mathbf{k}}^{pd})^{\dagger} & \hat{\mathcal{E}}_{\mathbf{k}}^{dd} \end{pmatrix}, \quad (4)$$

where

$$\hat{\mathcal{E}}_{\mathbf{k}}^{qq'} = \begin{pmatrix} \hat{\mathcal{E}}_{\mathbf{k}}^{qq'} & \hat{0} \\ \hat{0} & \hat{\mathcal{E}}_{\mathbf{k}}^{qq'} \end{pmatrix} \quad (q, q' = p \text{ or } d) \quad (5)$$

and

$$\hat{\lambda}_{\mathbf{k}} = \hat{\lambda}^{(0)} + \hat{\lambda}_{\mathbf{k}}^{(1)}. \quad (6)$$

Here, $\hat{\mathcal{E}}_{\mathbf{k}}^{qq'}$ and $\hat{\lambda}_{\mathbf{k}}$ are 6×6 matrices, while $\hat{\mathcal{E}}_{\mathbf{k}}^{pd}$ is a 3×3 matrix. $\hat{\mathcal{E}}_{\mathbf{k}}^{qq'}$ ($q, q' = p$ or d) represents usual hopping processes. $\hat{0}$ in eq. (5) is due to the fact that the non-relativistic Hamiltonian has no terms mixing the spin components. $\hat{\lambda}_{\mathbf{k}}$ represents the spin-orbit coupling that is caused by relativistic effects, and has matrix elements mixing the spin components. In the following subsections, we explain details of each matrix in order.

3.2.1 Spin-Orbit Coupling

First, $\hat{\lambda}_{\mathbf{k}}$ contains the contributions from the spin-orbit coupling on the Pb- p orbitals. $\hat{\lambda}^{(0)}$ represents the on-site $\mathbf{L} \cdot \mathbf{S}$ coupling for the p -orbitals and is explicitly

written as

$$\hat{\lambda}^{(0)} = \lambda_0 \begin{pmatrix} 0 & -i & 0 & 0 & 0 & 1 \\ i & 0 & 0 & 0 & 0 & -i \\ 0 & 0 & 0 & -1 & i & 0 \\ 0 & 0 & -1 & 0 & i & 0 \\ 0 & 0 & -i & -i & 0 & 0 \\ 1 & i & 0 & 0 & 0 & 0 \end{pmatrix}. \quad (7)$$

Next, $\hat{\lambda}_{\mathbf{k}}^{(1)}$ represents the intersite counterpart of the $\mathbf{L} \cdot \mathbf{S}$ coupling and is explicitly written as

$$\hat{\lambda}_{\mathbf{k}}^{(1)} = \lambda_1 \begin{pmatrix} 0 & -i\bar{c}_z & 0 & 0 & 0 & \bar{c}_y \\ i\bar{c}_z & 0 & 0 & 0 & 0 & -i\bar{c}_x \\ 0 & 0 & 0 & -\bar{c}_y & i\bar{c}_x & 0 \\ 0 & 0 & -\bar{c}_y & 0 & i\bar{c}_z & 0 \\ 0 & 0 & -i\bar{c}_x & -i\bar{c}_z & 0 & 0 \\ \bar{c}_y & i\bar{c}_x & 0 & 0 & 0 & 0 \end{pmatrix}, \quad (8)$$

where $\bar{c}_x = c_y + c_z$, $\bar{c}_y = c_z + c_x$, and $\bar{c}_z = c_x + c_y$ with $c_a = \cos k_a$ ($a = x, y, z$). Here the intersite coupling means the coupling between the nearest neighbor pair of two Pb- p orbitals. (Ca- d orbitals are not involved in this coupling.) $\hat{\lambda}_{\mathbf{k}}^{(1)}$ was neglected in ref. 12 since only $\hat{\lambda}^{(0)}$ plays an important role in reproducing the main features of the band structure obtained in the first-principles calculation. However, a close observation of the band structure reveals that the energy splittings between the states with $J = 1/2$ and $J = 3/2$ take different values at the Γ - and at the R-point, which can be explained only if we take account of $\hat{\lambda}_{\mathbf{k}}^{(1)}$. In the following formulation, we keep $\hat{\lambda}_{\mathbf{k}}^{(1)}$ in order to see its effect, although the actual magnitude of λ_1 in eq. (8) is small.

3.2.2 p - p matrix elements

Next, $\hat{\mathcal{E}}_{\mathbf{k}}^{pp}$ contains the on-site energy of the Pb- p orbital and hoppings between the two Pb- p orbitals. Considering all the hopping processes between the nearest- and the next-nearest-neighbor pairs of Pb- p orbitals as shown in Fig. 3(c), $\hat{\mathcal{E}}_{\mathbf{k}}^{pp}$ becomes

$$\hat{\mathcal{E}}_{\mathbf{k}}^{pp} = \begin{pmatrix} \epsilon_{xx} & \epsilon_{xy} & \epsilon_{xz} \\ \epsilon_{yx} & \epsilon_{yy} & \epsilon_{yz} \\ \epsilon_{zx} & \epsilon_{zy} & \epsilon_{zz} \end{pmatrix}, \quad (9)$$

where

$$\epsilon_{xx} = \epsilon_p + 2t_{p1}c_x + 2t_{p2}\bar{c}_x + 4t_{p3}c_y c_z + 4t_{p5}c_x \bar{c}_x, \quad (10a)$$

$$\epsilon_{yy} = \epsilon_p + 2t_{p1}c_y + 2t_{p2}\bar{c}_y + 4t_{p3}c_z c_x + 4t_{p5}c_y \bar{c}_y, \quad (10b)$$

$$\epsilon_{zz} = \epsilon_p + 2t_{p1}c_z + 2t_{p2}\bar{c}_z + 4t_{p3}c_x c_y + 4t_{p5}c_z \bar{c}_z, \quad (10c)$$

and $\epsilon_{xy} = -4t_{p4}s_x s_y$, $\epsilon_{yz} = -4t_{p4}s_y s_z$, and $\epsilon_{zx} = -4t_{p4}s_z s_x$ with $s_a = \sin k_a$ ($a = x, y, z$). Note that t_{p4} and t_{p5} were not included in ref. 12 for simplicity. These terms improve the agreement between the band structure of the tight-binding model and that of the first-principles calculation, although the results do not change qualitatively.

3.2.3 d - d matrix elements

Next, $\hat{\mathcal{E}}_{\mathbf{k}}^{dd}$ contains the on-site energy of the Ca- d orbital and hoppings between the two Ca- d orbitals. Considering up to the third-nearest-neighbor pairs of Ca- d

orbitals as shown in Fig. 3(d), $\hat{\mathcal{E}}_{\mathbf{k}}^{dd}$ becomes

$$\hat{\mathcal{E}}_{\mathbf{k}}^{dd} = \begin{pmatrix} \epsilon_{11} & \epsilon_{12} & \epsilon_{13} \\ \epsilon_{21} & \epsilon_{22} & \epsilon_{23} \\ \epsilon_{31} & \epsilon_{32} & \epsilon_{33} \end{pmatrix}, \quad (11)$$

where

$$\epsilon_{11} = \epsilon_d + 2t_{d1}c_x + 2t_{d2}\bar{c}_x, \quad (12a)$$

$$\epsilon_{22} = \epsilon_d + 2t_{d1}c_y + 2t_{d2}\bar{c}_y, \quad (12b)$$

$$\epsilon_{33} = \epsilon_d + 2t_{d1}c_z + 2t_{d2}\bar{c}_z, \quad (12c)$$

$$\epsilon_{12} = 4(t_{d0} + 2t_{d3}c_z)c_{\frac{y}{2}}c_{\frac{z}{2}}, \quad (12d)$$

$$\epsilon_{23} = 4(t_{d0} + 2t_{d3}c_x)c_{\frac{y}{2}}c_{\frac{z}{2}}, \quad (12e)$$

$$\epsilon_{31} = 4(t_{d0} + 2t_{d3}c_y)c_{\frac{x}{2}}c_{\frac{z}{2}}, \quad (12f)$$

with $c_{\frac{a}{2}} = \cos \frac{k_a}{2}$ ($a = x, y, z$). Note that t_{d3} was not included in ref. 12 again, and is included here for completeness and to improve the tight-binding model.

3.2.4 d - p matrix elements

Finally, $\hat{\mathcal{E}}^{pd}$ represents the hybridization between the nearest-neighbor pair of the Pb- p and the Ca- d orbitals, which is written as

$$\hat{\mathcal{E}}_{\mathbf{k}}^{pd} = \begin{pmatrix} 0 & \epsilon_{x2} & \epsilon_{x3} \\ \epsilon_{y1} & 0 & \epsilon_{y3} \\ \epsilon_{z1} & \epsilon_{z2} & 0 \end{pmatrix}, \quad (13)$$

where $\epsilon_{x2} = -4it_{dp}s_{\frac{y}{2}}c_{\frac{z}{2}}$, $\epsilon_{x3} = 4it_{dp}s_{\frac{z}{2}}c_{\frac{y}{2}}$, $\epsilon_{y3} = -4it_{dp}s_{\frac{z}{2}}c_{\frac{x}{2}}$, $\epsilon_{y1} = 4it_{dp}s_{\frac{y}{2}}c_{\frac{z}{2}}$, $\epsilon_{z1} = -4it_{dp}s_{\frac{x}{2}}c_{\frac{z}{2}}$, and $\epsilon_{z2} = 4it_{dp}s_{\frac{x}{2}}c_{\frac{y}{2}}$ with $s_{\frac{a}{2}} = \sin \frac{k_a}{2}$ ($a = x, y, z$).

3.3 Band Structure of the Tight-Binding Model

Parameters in $\hat{\mathcal{E}}_{\mathbf{k}}^{qq'}$ and $\hat{\lambda}_{\mathbf{k}}$ can be determined from the maximally localized Wannier function (MLWF) constructing method.^{25–27} However, we find that the parameter set obtained using MLWF, which includes rather long-ranged hopping processes, does not reproduce the band structure near the Fermi energy if the hopping integrals are truncated as in Figs. 3(c) and 3(b). This is because the long-ranged hopping processes in MLWF are important for Pb- p orbitals since their wave functions have large spreadings, while the hopping integrals in Figs. 3(c) and 3(b) are relatively short-ranged. In order to overcome this problem, we modify some parameters obtained in MLWF to reproduce the band structure. This simplification gives no significant problems in the following arguments of the appearance of the Dirac electron.

The determined parameters are $\epsilon_p = -1.462$, $t_{p1} = 0.290$, $t_{p2} = 0.045$, $t_{p3} = 0.035$, $t_{p4} = 0.0791$, $t_{p5} = 0.055$, $\epsilon_d = 2.146$, $t_{d0} = 0.349$, $t_{d1} = 0.184$, $t_{d2} = -0.195$, $t_{d3} = 0.047$, $t_{dp} = 0.302$, $\lambda_0 = 0.330$, and $\lambda_1 = 0.015$ (the units are eV). Figure 4(a) illustrates the band structure in this tight-binding model compared with the results of the first-principles calculation. Comparing Fig. 4(a) and Figs. 2(c) and 2(e), we can see that the tight-binding model well reproduces the bands with large Ca- $d_{x^2-y^2}$ [Fig. 2(c)] and Pb- p [Fig. 2(e)] orbital weights. This is natural since we have taken account of these orbitals in constructing the tight-binding model. Note that not only

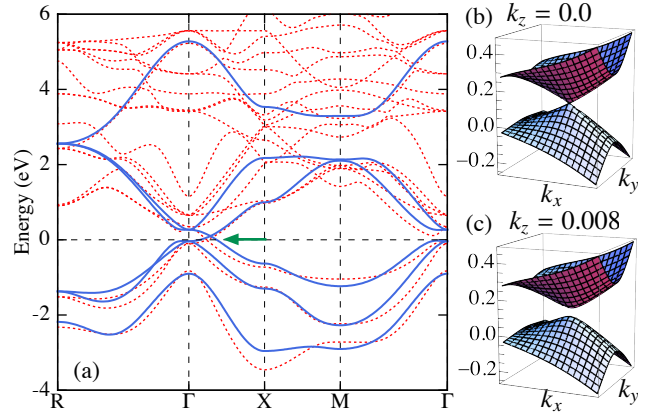


Fig. 4. (Color online) (a) Band structure of the tight-binding model (solid lines) and that obtained in the first-principles calculation (dotted lines). (b,c) Dispersion relations of the tight-binding model around a Dirac point. k_x and k_y are in the region of $0.06 \leq k_x \leq 0.22$ and $-0.08 \leq k_y \leq 0.08$, respectively, while k_z is 0 (b), and 0.008 (c). Momenta are represented in the unit of $2\pi/a$ where a is the cubic lattice constant.

the global band structure, but also the most important feature of this system, i.e., the Dirac type linear dispersion in the vicinity of the Fermi energy, is captured.

In order to check this point, Figs. 4(b) and 4(c) provide three-dimensional plots of the dispersion relations of the tight-binding model around one of the Dirac points, $(k_0, 0, 0)$. Figure 4(b) for $k_z = 0$ shows that two cone-shaped bands touch with each other at an isolated point in the k_x - k_y plane, while Fig. 4(c) shows that a gap emerges between the two bands as k_z becomes finite. These observations confirm the existence of a three-dimensional Dirac electron in this model. However, we find that the Dirac electron in this tight-binding model is *massless* while the first-principles calculation gives a small mass gap of 15 meV. We find that this mass term originates from the contribution from the other orbitals which are not included in the present tight-binding model. This will be discussed later in §4.4.

4. Low-Energy Effective Hamiltonian

In this section, we concentrate on the Dirac point on the k_z -axis, namely, the Dirac point at $(0, 0, k_0)$. This is because we are familiar with choosing the z -axis as the quantization axis of the spin. When we discuss the band structure around other Dirac points, such as $(k_0, 0, 0)$, it is convenient to direct the spin quantization axis along the x -axis.

4.1 Analysis of the Tight-Binding Model

In order to prove that the low-energy effective Hamiltonian of this material is really a Dirac Hamiltonian, we first introduce a new basis set. Here, the eigenstates at the Γ -point are taken as the new basis set since the Dirac point under consideration is relatively close to the Γ -point. In addition, the high symmetry of the Γ -point allows us to classify the eigenstates easily. Explicitly, the

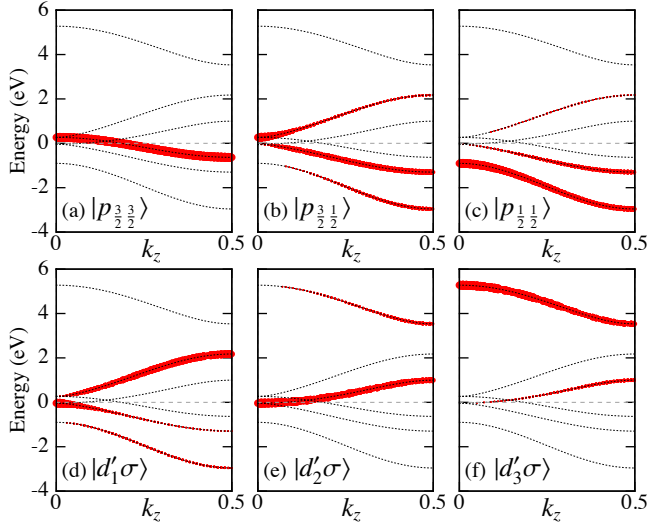


Fig. 5. (Color online) Weight distributions of the new basis states on the bands along the k_z -axis. (a)–(f) show the weights of $|p_{\frac{3}{2}\frac{3}{2}}^{\uparrow}\rangle$, $|p_{\frac{3}{2}\frac{1}{2}}^{\uparrow}\rangle$, $|p_{\frac{1}{2}\frac{1}{2}}^{\uparrow}\rangle$, $|d'_1\sigma\rangle$, $|d'_2\sigma\rangle$, and $|d'_3\sigma\rangle$, respectively.

new basis wave functions are defined as

$$|p_{\frac{3}{2}\frac{3}{2}}^{\uparrow}\rangle = -\frac{1}{\sqrt{2}}(|p_x \uparrow\rangle + i|p_y \uparrow\rangle), \quad (14a)$$

$$|p_{\frac{3}{2}\frac{1}{2}}^{\uparrow}\rangle = -\frac{1}{\sqrt{6}}(|p_x \downarrow\rangle + i|p_y \downarrow\rangle - 2|p_z \uparrow\rangle), \quad (14b)$$

$$|p_{\frac{3}{2}\frac{1}{2}}^{\downarrow}\rangle = \frac{1}{\sqrt{6}}(|p_x \uparrow\rangle - i|p_y \uparrow\rangle + 2|p_z \downarrow\rangle), \quad (14c)$$

$$|p_{\frac{3}{2}\frac{3}{2}}^{\downarrow}\rangle = \frac{1}{\sqrt{2}}(|p_x \downarrow\rangle - i|p_y \downarrow\rangle), \quad (14d)$$

$$|p_{\frac{1}{2}\frac{1}{2}}^{\uparrow}\rangle = \frac{1}{\sqrt{3}}(|p_x \downarrow\rangle + i|p_y \downarrow\rangle + |p_z \uparrow\rangle), \quad (14e)$$

$$|p_{\frac{1}{2}\frac{1}{2}}^{\downarrow}\rangle = \frac{1}{\sqrt{3}}(|p_x \uparrow\rangle - i|p_y \uparrow\rangle - |p_z \downarrow\rangle), \quad (14f)$$

and

$$|d'_1\sigma\rangle = \frac{1}{\sqrt{2}}(|d_1\sigma\rangle - |d_2\sigma\rangle), \quad (15a)$$

$$|d'_2\sigma\rangle = \frac{1}{\sqrt{6}}(|d_1\sigma\rangle + |d_2\sigma\rangle - 2|d_3\sigma\rangle), \quad (15b)$$

$$|d'_3\sigma\rangle = \frac{1}{\sqrt{3}}(|d_1\sigma\rangle + |d_2\sigma\rangle + |d_3\sigma\rangle). \quad (15c)$$

Here, $|p_{JJ_z}\rangle$ is just the wave function having a total angular momentum J with its z -component J_z realized from the on-site spin-orbit coupling of the Pb- p orbitals. The bases $|d'_1\sigma\rangle$, $|d'_2\sigma\rangle$, and $|d'_3\sigma\rangle$ originate from the Ca- d orbitals [eq. (15)], and spin up and spin down components are not mixed since the spin-orbit coupling on the Ca atoms is neglected in this model.

Figure 5 shows the weight distribution of the new basis states on the bands along the k_z -axis. From this figure, it is clearly seen that the bands crossing the Fermi energy and forming the Dirac electron come from the $|p_{\frac{3}{2}\frac{3}{2}}^{\uparrow}\rangle$ and $|d'_2\sigma\rangle$ states. Therefore, it will be enough to keep only the four states $|p_{\frac{3}{2}\frac{3}{2}}^{\uparrow}\rangle$, $|p_{\frac{3}{2}\frac{3}{2}}^{\downarrow}\rangle$, $|d'_2 \uparrow\rangle$, and $|d'_2 \downarrow\rangle$ out of 12 states

in eqs. (14) and (15) in deriving the low-energy effective Hamiltonian. When we examine Fig. 5 more closely, we can see that a small weight of $|d'_3\sigma\rangle$ state is mixed in the band forming the Dirac electron [Fig. 5(f)]. However, the mixed weight is so small that it gives no harm in the following arguments.

4.2 Expansion around Dirac point

Reflecting the arguments in the previous subsection, we derive the low-energy effective Hamiltonian in the following two-step process. In the first step, the matrix elements of $\hat{\mathcal{E}}_{\mathbf{k}}^{qq'}$ are expanded with respect to k_x and k_y up to the first order (remember that we are concentrating on the Dirac point on the k_z -axis), and at the same time, the basis set in eq. (1) is transformed into that in eqs. (14) and (15). In the second step, matrix elements irrelevant to $|p_{\frac{3}{2}\frac{3}{2}}^{\uparrow}\rangle$, $|p_{\frac{3}{2}\frac{3}{2}}^{\downarrow}\rangle$, $|d'_2 \uparrow\rangle$, and $|d'_2 \downarrow\rangle$ are dropped. This procedure is slightly different from that used in ref. 12, but the two procedures are essentially the same. In the following, we make use of the notation $k_{\pm} = k_x \pm ik_y$.

In the first step, i.e., expanding the matrix elements with respect to k_x and k_y (or k_{\pm}), and changing the basis set, $\hat{\mathcal{E}}_{\mathbf{k}}$ is transformed as

$$\hat{\mathcal{E}}'_{\mathbf{k}} = \begin{pmatrix} \hat{\mathcal{E}}_{\mathbf{k}}^{pp} & \hat{\mathcal{E}}_{\mathbf{k}}^{d'p} \\ (\hat{\mathcal{E}}_{\mathbf{k}}^{d'p})^{\dagger} & \hat{\mathcal{E}}_{\mathbf{k}}^{d'd} \end{pmatrix}. \quad (16)$$

Here, $\hat{\mathcal{E}}_{\mathbf{k}}^{pp}$ can be explicitly written as

$$\hat{\mathcal{E}}_{\mathbf{k}}^{pp} = \begin{pmatrix} g_1 & g_5 k_- & 0 & 0 & g'_5 k_- & 0 \\ g_5 k_+ & g_2 & 0 & 0 & g_4 & -g''_5 k_- \\ 0 & 0 & g_2 & -g_5 k_- & -g''_5 k_+ & -g_4 \\ 0 & 0 & -g_5 k_+ & g_1 & 0 & g'_5 k_+ \\ g'_5 k_+ & g_4 & -g''_5 k_- & 0 & g_3 & 0 \\ 0 & -g''_5 k_+ & -g_4 & g'_5 k_- & 0 & g_3 \end{pmatrix} \quad (17)$$

with

$$g_1 = \lambda_0 + 2\lambda_1 + f_0, \quad (18a)$$

$$g_2 = \lambda_0 + \frac{2}{3}\lambda_1(1 + 2c_z) + \frac{1}{3}(f_0 + 2f_1), \quad (18b)$$

$$g_3 = -2\lambda_0 - \frac{4}{3}\lambda_1(2 + c_z) + \frac{1}{3}(2f_0 + f_1), \quad (18c)$$

$$g_4 = \frac{\sqrt{2}}{3}\lambda_1(1 - c_z) - \frac{\sqrt{2}}{3}(f_0 - f_1), \quad (18d)$$

$$g_5 = 4t_{p4}s_z/\sqrt{3}, \quad (18e)$$

and $g'_5 = g_5/\sqrt{2}$, $g''_5 = \sqrt{3}g'_5$, and

$$f_0 = (\epsilon_p + 2t_{p1}) + (2t_{p2} + 4t_{p5})(1 + c_z) + 4t_{p3}c_z, \quad (19a)$$

$$f_1 = (\epsilon_p + 4t_{p2} + 4t_{p3}) + (2t_{p1} + 8t_{p5})c_z. \quad (19b)$$

On the other hand, $\hat{\mathcal{E}}_{\mathbf{k}}^{d'd}$ can be explicitly written as

$$\hat{\mathcal{E}}_{\mathbf{k}}^{d'd} = \begin{pmatrix} g_6 & 0 & 0 & 0 & 0 & 0 \\ 0 & g_7 & g_9 & 0 & 0 & 0 \\ 0 & g_9 & g_8 & 0 & 0 & 0 \\ 0 & 0 & 0 & g_6 & 0 & 0 \\ 0 & 0 & 0 & 0 & g_7 & g_9 \\ 0 & 0 & 0 & 0 & g_9 & g_8 \end{pmatrix} \quad (20)$$

with

$$g_6 = f_3 - f_5, \quad (21a)$$

$$g_7 = \frac{1}{3}(f_3 + 2f_4 + f_5 - 4f_6), \quad (21b)$$

$$g_8 = \frac{1}{3}(2f_3 + f_4 + 2f_5 + 4f_6), \quad (21c)$$

$$g_9 = \frac{\sqrt{2}}{3}(f_3 - f_4 + f_5 - f_6), \quad (21d)$$

and

$$f_3 = (\epsilon_d + 2t_{d1} + 2t_{d2}) + 2t_{d2}c_z, \quad (22a)$$

$$f_4 = (\epsilon_d + 4t_{d2}) + 2t_{d1}c_z, \quad (22b)$$

$$f_5 = 4(t_{d0} + 2t_{d3}c_z), \quad (22c)$$

$$f_6 = 4(t_{d0} + 2t_{d3})c_{\frac{z}{2}}. \quad (22d)$$

The off-diagonal matrix, $\hat{\mathcal{E}}_{\mathbf{k}}^{idp}$, is expressed as

$$\hat{\mathcal{E}}_{\mathbf{k}}^{idp} = \begin{pmatrix} -h_1k_- & h_2k_+ & h_3k_+ & 0 & 0 & 0 \\ -h_4 & 0 & 0 & -h'_1k_- & h'_2k_+ & h'_3k_+ \\ -h'_1k_+ & -h'_2k_- & -h'_3k_- & -h_4 & 0 & 0 \\ 0 & 0 & 0 & -h_1k_+ & -h_2k_- & -h_3k_- \\ -h'_4 & 0 & 0 & h''_1k_- & -h''_2k_+ & -h''_3k_+ \\ h''_1k_+ & -h''_2k_- & -h''_3k_- & h'_4 & 0 & 0 \end{pmatrix}, \quad (23)$$

with $h_1 = it_{dp}c_{\frac{z}{2}}$, $h_2 = it_{dp}(2 + c_{\frac{z}{2}})/\sqrt{3}$, $h_3 = -2it_{dp}(1 - c_{\frac{z}{2}})/\sqrt{6}$, and $h_4 = 8it_{dp}s_{\frac{z}{2}}/\sqrt{3}$, where $h'_{1,2,3} = h_{1,2,3}/\sqrt{3}$, $h''_{1,2,3} = \sqrt{2}h'_{1,2,3}$, and $h'_4 = h_4/\sqrt{2}$.

In the second step, we keep only the matrix elements related to $|p_{\frac{3}{2}\frac{3}{2}}\rangle$, $|p_{\frac{3}{2}\frac{1}{2}}\rangle$, $|d'_2\uparrow\rangle$, and $|d'_2\downarrow\rangle$, and drop all the other matrix elements. As a result, the Hamiltonian is transformed to a 4×4 matrix $\hat{\mathcal{E}}_{\mathbf{k}}''$, which can be written as

$$\hat{\mathcal{E}}_{\mathbf{k}}'' = \begin{pmatrix} g_1 & 0 & h_2k_+ & 0 \\ 0 & g_1 & 0 & -h_2k_- \\ h_2^*k_- & 0 & g_7 & 0 \\ 0 & -h_2^*k_+ & 0 & g_7 \end{pmatrix}. \quad (24)$$

Finally, suppose that $g_1 = g_7$ is satisfied at some $k_z = k_0$, and expand g_1 and g_7 as

$$g_1 = -c_p\delta k_z + \epsilon_0, \quad g_7 = c_d\delta k_z + \epsilon_0 \quad (25)$$

where $\delta k_z = k_z - k_0$ and $\epsilon_0 = g_1 (= g_7)$ at $k_z = k_0$. Substituting eq. (25) into eq. (24), the Hamiltonian becomes,

$$\begin{aligned} \hat{\mathcal{E}}_{\mathbf{k}}''' &= \epsilon_0\hat{1} + \begin{pmatrix} -c_p\delta k_z & 0 & -h_2k_+ & 0 \\ 0 & -c_p\delta k_z & 0 & h_2k_- \\ -h_2^*k_- & 0 & c_d\delta k_z & 0 \\ 0 & h_2^*k_+ & 0 & c_d\delta k_z \end{pmatrix} \\ &= (\epsilon_0 + \delta c\delta k_z)\hat{1} + \begin{pmatrix} -c\delta k_z & 0 & -h_2k_+ & 0 \\ 0 & -c\delta k_z & 0 & h_2k_- \\ -h_2^*k_- & 0 & c\delta k_z & 0 \\ 0 & h_2^*k_+ & 0 & c\delta k_z \end{pmatrix}, \end{aligned} \quad (26)$$

where c and δc are defined as $c = (c_d + c_p)/2$ and $c = (c_d - c_p)/2$. At this point, it is easy to demonstrate that eq. (26) is really a (tilted) massless Dirac Hamiltonian

by changing the order of the rows and columns. Here, we emphasize that the four basis states of this Dirac Hamiltonian come from $|p_{\frac{3}{2}\frac{3}{2}}\rangle$, $|p_{\frac{3}{2}\frac{1}{2}}\rangle$, $|d'_2\uparrow\rangle$, and $|d'_2\downarrow\rangle$.

In deriving eq. (24), we have neglected the states $|p_{\frac{3}{2}\frac{1}{2}}\rangle$, $|p_{\frac{3}{2}\frac{3}{2}}\rangle$, $|p_{\frac{1}{2}\frac{1}{2}}\rangle$, and $|d'_1\sigma\rangle$. Here, let us discuss why we can neglect these states in detail. Firstly, the energies of these states are away from the energy of the Dirac point (ϵ_0). For $|p_{\frac{1}{2}\frac{1}{2}}\rangle$ and $|p_{\frac{3}{2}\frac{1}{2}}\rangle$, this is mainly because $|g_3 - \epsilon_0|$ is large at $k_z = k_{z0}$. For $|p_{\frac{3}{2}\frac{1}{2}}\rangle$, $|p_{\frac{3}{2}\frac{3}{2}}\rangle$, and $|d'_1\sigma\rangle$, this is due to the term h_4 in eq. (23). Namely, although $|g_2 - \epsilon_0|$ and $|g_6 - \epsilon_0|$ at $k_z = k_{z0}$ are not so large, the term h_4 , which is finite even for $|k_{\pm}| = 0$, makes eigenenergies for $|p_{\frac{3}{2}\frac{1}{2}}\rangle$, $|p_{\frac{3}{2}\frac{3}{2}}\rangle$, and $|d'_1\sigma\rangle$ away from ϵ_0 . Secondly, we find that the matrix elements between these states and the states that we have kept in eq. (23) are at most in the first order in k_{\pm} . This means that the contributions of these states to the low-energy Hamiltonian are at least in the second order in k_{\pm} .

On the other hand, we should be careful in neglecting $|d'_3\sigma\rangle$, since the matrix elements between $|d'_3\sigma\rangle$ and $|d'_2\sigma\rangle$ are finite even for $|k_{\pm}| = 0$ [see eq. (23)]. In order to eliminate these constant off-diagonal matrix elements, we have to choose an appropriate linear combination of $|d'_2\sigma\rangle$ and $|d'_3\sigma\rangle$ instead of pure $|d'_2\sigma\rangle$ as a basis state. However, using such a linear combination only results in a renormalization of $h_{2,3}$, $h'_{2,3}$, and $h''_{2,3}$ in eq. (23) since the transformation leading to the linear combination of $|d'_2\sigma\rangle$ and $|d'_3\sigma\rangle$ only mixes the second and the third columns (or the fifth and the sixth columns) of the matrix in eq. (23). As a result, the low-energy effective Hamiltonian should have the same form as eq. (24). Furthermore, the weight of $|d'_3\sigma\rangle$ mixed in the band forming the Dirac electron is very small as we have seen in Fig. 5(f).

4.3 Origin of the Dirac Electron

As we discussed in ref. 12, the origin of the Dirac electron in this model can be clarified by considering the effects of the hybridization between the p- and d-bands (t_{dp}) on the band structure. As we have pointed out, the top of p-bands locates above the bottom of d-bands. Then, if the hybridization t_{dp} is neglected, the p- and d-bands should form usual hole- and electron-like Fermi surfaces around the Γ -point, and there appear no Dirac electrons. Although the p- and d-bands cross, the crossing points are not isolated points in the Brillouin zone. Then, we consider the effect of finite t_{dp} . In general, finite t_{dp} causes the band anticrossing of the p- and d-bands, and eliminates the crossing points between the p- and d-bands. However, in the present model, the band anticrossing does not occur on the Γ -X line because of the symmetry of wave functions (ref. 12 and see below). Consequently, the crossing points are left on the special and isolated points in the Brillouin zone that are located on the Γ -X line. This means that there emerge Dirac points in this model. Note that these arguments have some similarities with those in ref.28.

Finally, we address why the band anticrossing does not occur on the Γ -X line. For simplicity, we concentrate on

the Dirac point on the k_z -axis, which is one of the Γ -X line. In this case, the states relevant to the Dirac electron are $|p_{\frac{3}{2}\frac{3}{2}}\rangle$, $|p_{\frac{3}{2}\frac{3}{2}}\rangle$, and $|d'_2\sigma\rangle$. As defined in eqs. (14) and (15), $|p_{\frac{3}{2}\frac{3}{2}}\rangle$ and $|p_{\frac{3}{2}\frac{3}{2}}\rangle$ are the superpositions of $|p_x\sigma\rangle$ and $|p_y\sigma\rangle$, while $|d'_2\sigma\rangle$ is a superposition of $|d_1\sigma\rangle$, $|d_2\sigma\rangle$, and $|d_3\sigma\rangle$. The latter wave functions schematically depicted in Figs. 6(a) and 6(b). From Fig. 6, it is apparent that $|p_x\sigma\rangle$ (or $|p_y\sigma\rangle$) cannot hybridize with the wave functions of Figs. 6(a) and 6(b) by a symmetrical reason. This means that there are no matrix elements between $|p_{\frac{3}{2}\frac{3}{2}}\rangle$ (or $|p_{\frac{3}{2}\frac{3}{2}}\rangle$) and $|d'_2\sigma\rangle$ on the k_z -axis, which explains the absence of the band anticrossing. Note that if a momentum is off from the k_z -axis, there appear finite matrix elements between $|p_{\frac{3}{2}\frac{3}{2}}\rangle$ (or $|p_{\frac{3}{2}\frac{3}{2}}\rangle$) and $|d'_2\sigma\rangle$.

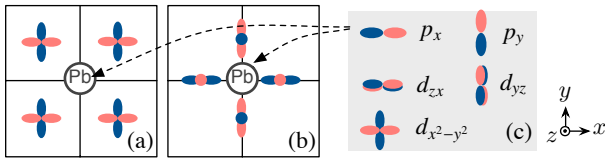


Fig. 6. (Color online) (a,b) The wave functions involved in $|d'_2\sigma\rangle$ states for the case that the momentum is on the k_z -axis. (c) Schematic pictures for the orbitals on the Pb site.

4.4 Origin of the Mass Term

The above arguments nicely explain the origin of the massless Dirac electron in the tight-binding model. However, the first-principles calculation shows that there exists a small but finite mass gap at the Dirac point in Ca_3PbO . In this subsection, we clarify the origin of this mass term. First, let us check the irreducible representations to which the bands on the Γ -X line belong. As shown in Fig. 7, it turns out that the two bands forming the Dirac electron belong to the same irreducible representation Γ_7 . If they belong to different representations, it is impossible to have a mass gap. However, since they belong to the same representation, finite matrix elements between these two bands can exist, which result in a finite mass gap.

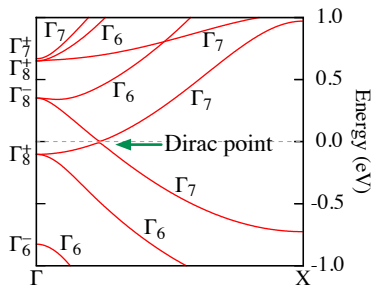


Fig. 7. (Color online) Irreducible representations of the bands on the Γ -X line. The notations used in ref. 29 are used to label irreducible representations.

Since the mass term is very small in Ca_3PbO , we think

that the simple tight-binding model introduced in the previous subsection is a good starting point discussing the mass term. In order to include the small mass term to the effective model, some minor effects should be included. In the following, we consider the effects caused by the orbitals not included in the previous subsection. As a representative example, we add the Pb-5d orbitals to the basis set. (The inclusion of other orbitals leads to the similar conclusion.) Since these orbitals are located far away from the Fermi energy (about -15 eV below the Fermi energy according to the first-principles calculation), we treat these orbitals in a perturbative way. We concentrate on the effective model around the Dirac point on the k_z -axis as before in the subsequent arguments.

The Pb-5d orbitals considered here are also shown in Fig. 6(c). From Fig. 6(c), we can see that Pb- d_{zx} (Pb- d_{yz}) can hybridize with $|p_x\sigma\rangle$ ($|p_y\sigma\rangle$) in the z -direction if k_z is finite. As a result, $|p_{\frac{3}{2}\frac{3}{2}}\rangle$, and $|p_{\frac{3}{2}\frac{3}{2}}\rangle$, which are relevant to the Dirac electron, can hybridize with Pb- d_{zx} and Pb- d_{yz} , since they are composed of $|p_x\sigma\rangle$ and $|p_y\sigma\rangle$. On the other hand, we can see that Pb- $d_{x^2-y^2}$ orbital can hybridize with the wave functions depicted in Figs. 6(a) and 6(b). As a result, $|d'_2\sigma\rangle$, which is the other state relevant to the Dirac electron and is composed of wave functions in Figs. 6(a) and 6(b), can hybridize with Pb- $d_{x^2-y^2}$ orbital. To summarize, $|p_{\frac{3}{2}\frac{3}{2}}\rangle$, $|p_{\frac{3}{2}\frac{3}{2}}\rangle$, and $|d'_2\sigma\rangle$ will be modified in a perturbative way as

$$|p_{\frac{3}{2}\frac{3}{2}}\rangle \longrightarrow |p_{\frac{3}{2}\frac{3}{2}}\rangle + \frac{w_1}{\Delta_1} |\text{Pb-}d_{\frac{3}{2}}\rangle \quad (27)$$

$$|p_{\frac{3}{2}\frac{3}{2}}\rangle \longrightarrow |p_{\frac{3}{2}\frac{3}{2}}\rangle + \frac{w_1}{\Delta_1} |\text{Pb-}d_{\frac{3}{2}}\rangle \quad (28)$$

$$|d'_2\sigma\rangle \longrightarrow |d'_2\sigma\rangle + \frac{w_2}{\Delta_2} |\text{Pb-}d_{x^2-y^2}\sigma\rangle, \quad (29)$$

where

$$|\text{Pb-}d_{\frac{3}{2}}\rangle = -\frac{1}{\sqrt{2}} \left(|\text{Pb-}d_{zx}\uparrow\rangle + i|\text{Pb-}d_{yz}\uparrow\rangle \right), \quad (30)$$

$$|\text{Pb-}d_{\frac{3}{2}}\rangle = \frac{1}{\sqrt{2}} \left(|\text{Pb-}d_{zx}\downarrow\rangle - i|\text{Pb-}d_{yz}\downarrow\rangle \right). \quad (31)$$

Here, $w_{1,2}$ and $\Delta_{1,2}$ represent the matrix elements and the level differences between the originally included and newly added orbitals, respectively. Note that w_1 and w_2 depend on k_z , and w_1 is zero at $k_z = 0$ while w_2 is finite at $k_z = 0$ from the symmetry of the orbitals.

Now, assuming the standard on-site $\mathbf{L} \cdot \mathbf{S}$ coupling for Pb 5d orbitals (not Pb 6p orbitals), there appear new matrix elements between $|p_{\frac{3}{2}\frac{3}{2}}\rangle$, $|p_{\frac{3}{2}\frac{3}{2}}\rangle$, and $|d'_2\sigma\rangle$ orbitals. Explicitly, we find that

$$\langle d'_2\uparrow | \hat{H}_{\text{LS}} | p_{\frac{3}{2}\frac{3}{2}}\rangle \sim \alpha \langle \text{Pb-}d_{x^2-y^2}\uparrow | \hat{H}_{\text{LS}} | \text{Pb-}d_{\frac{3}{2}}\rangle = 0, \quad (32a)$$

$$\langle d'_2\uparrow | \hat{H}_{\text{LS}} | p_{\frac{3}{2}\frac{3}{2}}\rangle \sim \alpha \langle \text{Pb-}d_{x^2-y^2}\uparrow | \hat{H}_{\text{LS}} | \text{Pb-}d_{\frac{3}{2}}\rangle = \sqrt{2}\alpha\lambda, \quad (32b)$$

where $\alpha = \frac{w_1 w_2}{\Delta_1 \Delta_2}$. Similarly, we have $\langle d'_2\downarrow | \hat{H}_{\text{LS}} | p_{\frac{3}{2}\frac{3}{2}}\rangle \sim \sqrt{2}\alpha\lambda$ and $\langle d'_2\downarrow | \hat{H}_{\text{LS}} | p_{\frac{3}{2}\frac{3}{2}}\rangle = 0$. Then, adding these con-

tributions to eq. (26), the effective Hamiltonian becomes

$$\hat{\mathcal{E}}_{\mathbf{k}}''' = (\epsilon_0 + \delta c \delta k_z) \hat{1} + \begin{pmatrix} -c\delta k_z & 0 & -h_2 k_+ & m \\ 0 & -c\delta k_z & m & h_2 k_- \\ -h_2^* k_- & m & c\delta k_z & 0 \\ m & h_2^* k_+ & 0 & c\delta k_z \end{pmatrix}, \quad (33)$$

with $m \sim \sqrt{2}\alpha\lambda$. This is nothing but a (tilted) massive Dirac Hamiltonian.

We can obtain the two important features about the mass term from the above derivation. First, the mass term is small since it requires the inclusion of the orbitals locating far away from the Fermi energy. Second, the mass term scales with the coefficient for the spin-orbit coupling, λ .

We must note that any other orbitals having the same symmetry as Pb- d_{zx} , d_{yz} , $d_{x^2-y^2}$ orbitals can be sources of the mass term. For example, some states originated from the Ca-3d orbitals (other than $d_{x^2-y^2}$, which is included in the original basis set) have symmetries of Pb- d_{zx} , and d_{yz} orbitals. Thus, inclusion of the Ca-3d orbitals other than $d_{x^2-y^2}$ will also contribute to the mass term. Again, these orbitals are located away from the Fermi energy, and thus, the mass term induced by these orbitals are also small. The resultant mass term scales with λ also in this case.

5. Topological Property and the Surface Band Structure

5.1 Topological Property

In this subsection, we discuss the relation of Ca_3PbO to the topological insulator. As we have stated, the top of p-bands, whose wave functions have odd parity at the Γ -point, locates above the bottom of d-bands, whose wave functions have even parity at the Γ -point. This kind of structure, i.e., an overlap of the two bands with opposite parity, is called an “inverted” band structure, which can lead to a topological insulator in some cases.^{30,31} Furthermore, Pb atom has a very strong spin-orbit coupling. Then, it is tempting to assign Ca_3PbO as a topological insulator. In fact, Ca_3PbO and its relatives are suggested as potential topological insulators in ref. 32. However, unfortunately, Ca_3PbO is not a topological insulator as explained in the following.

The Z_2 topological number ν_0 for Ca_3PbO is readily evaluated since this material has an inversion symmetry. According to ref. 30, ν_0 can be obtained from the formula

$$(-1)^{\nu_0} = \prod_{i=1}^8 \delta_i = \prod_{i=1}^8 \prod_{m=1}^N \xi_{2m}(\Gamma_i), \quad (34)$$

for the materials having an inversion symmetry. In this formula, Γ_i represents the time reversal invariant momenta (TRIM) in the Brillouin zone and $\xi_{2m}(\Gamma_i)$ represents the parity of the wave function for the $2m$ -th state at Γ_i . N is the number of filled bands counted neglecting the Kramers degeneracy. For the simple cubic crystal of Ca_3PbO , TRIM are the Γ -, X-, M-, and R-points where there are three X- and M-points. Using WIEN2k package, we derive the irreducible representations and the parities of the states at TRIM. Here, we concentrate on the states whose energies are in between -4 eV and 0 eV, since the

bands below -4 eV are associated with the completely filled shells of the involved atoms such as O-2p orbitals and give only trivial contributions to ν_0 . There are three bands between -4 eV and 0 eV, and thus, $N = 3$. The obtained results are summarized in Table I. From the table, we can see that the right hand side of eq. (34) is equal to 1, which implies that this material is topologically trivial.

Table I. Irreducible representations and the parities of the states whose energies are in between -4 eV and 0 eV at TRIM.

Γ_i	irreducible rep.	ξ_2	ξ_4	ξ_6	δ_i
$\Gamma (\times 1)$	Γ_6^- Γ_8^+	-	+	+	-
X ($\times 3$)	Γ_6^- Γ_6^- Γ_7^-	-	-	-	-
M ($\times 3$)	Γ_6^- Γ_7^- Γ_6^-	-	-	-	-
R ($\times 1$)	Γ_6^- Γ_8^-	-	-	-	-

We can understand why Ca_3PbO is topologically trivial as follows. As we have checked, there exists an “inverted” band structure at the Γ -point. However, the inverted bands at the Γ -point have a double degeneracy *other than* Kramers degeneracy. In other words, they have a quadruple degeneracy if the Kramers degeneracy is included. As a result, this “inverted” band structure gives $(-1)^2 = 1$ in the right hand side of eq. (34). This makes Ca_3PbO topologically trivial. In order to turn this material into a topological insulator, at least the degeneracy at the Γ -point should be lifted by lowering the symmetry of the crystal.

5.2 Surface Band Structure

Although we have proved that Ca_3PbO is not a topological insulator, we study the surface band structure of Ca_3PbO . The surface band structures are calculated using the tight-binding model in a slablike lattice structure having two (top and bottom) surfaces. Here, surfaces are treated as simple terminations of the lattice points for simplicity (i.e., we use open boundary conditions). In the following, we consider the cases in which the slab has 001 or 111 surface. In Ca_3PbO , there are two types of 001 surfaces. The schematic pictures for these two 001 surfaces are shown in Fig. 8(c) and 8(d). These two types of surfaces are named as 001A [Fig. 8(c)] and 001B [Fig. 8(d)], respectively. As we can see from Figs. 8(c) and 8(d), 001A surface has equal number of Ca and Pb sites, while 001B surface has only Ca sites. (In Fig. 8(d), O sites are also written, but O sites are not included in the basis set of the tight-binding model.) In contrast, there is only one type of 111 surface [Fig. 9(b)]. Actually, there is another possible 111 surface, but that surface has only O sites and is equivalent to the 111 surface in Fig. 9(b).

The surface band structures for the 001 surfaces are summarized in Figs. 8(a)–8(c). The top and bottom surfaces of the slab used in the calculation are 001A for Fig. 8(a), 001B for Fig. 8(b), and 001A and 001B for Fig. 8(c). Figure 8(f) shows the surface Brillouin zone for the 001 surface and the arrows indicate the path on which the band structures in Figs. 8(a)–8(c) are shown.

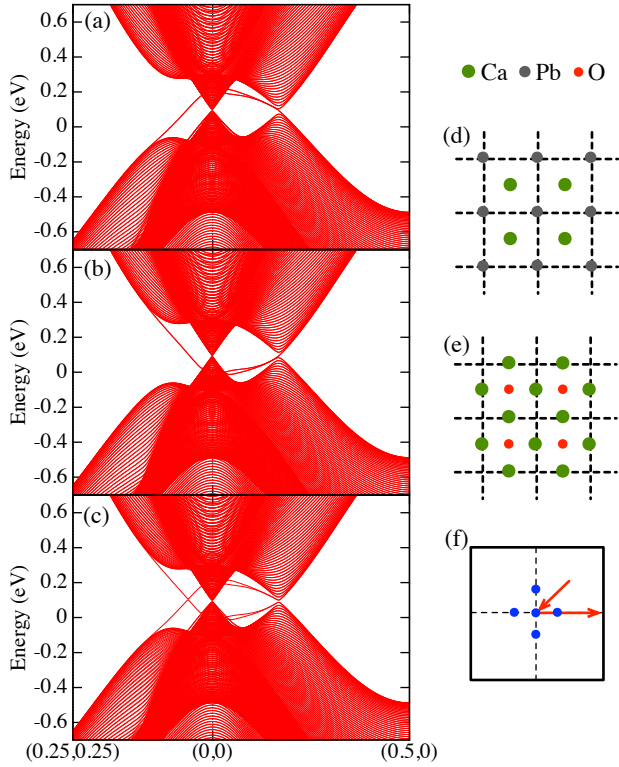


Fig. 8. (Color online) Surface band structures for the 001 surfaces. The top and bottom surfaces of the slab are (a) 001A, (b) 001B, and (c) 001A and 001B. (d,e) Schematic pictures for (d) 001A and (e) 001B surfaces. (f) Surface Brillouin zone for the 001 surfaces. Dots represent the Dirac points projected to the surface Brillouin zone. Arrows represent the path on which the band structure is plotted.

The positions of the Dirac points projected on to the surface Brillouin zone are represented by dots. Considering the relation between the arrows and dots in Fig. 8(f), the shapes of the bulk continuum (the region filled by a large number of bands) in Figs. 8(a)–8(c) are easily understood: the bulk continuum has a gap except near the projected Dirac points.

Very interestingly, we can see that several bands appear near $(0,0)$ in all of Figs. 8(a)–8(c) apart from the bulk continuum. We can see that these separated bands are definitely surface states since they are affected by the choice of the surfaces. When we closely investigate the surface states, we find that they are doubly degenerate in Figs. 8(a) and 8(b). This degeneracy is a Kramers degeneracy since the slab used in Figs. 8(a) and 8(b) has an inversion center because the top and bottom surfaces are identical. On the other hand, the surface states in Fig. 8(c) are nondegenerate. This is because the slab does not have an inversion center since the top and bottom surfaces are different for Fig. 8(c). From these results, we can see that the nondegenerate surface states exist when we look at one of the top or bottom surface. In this sense, this model resembles to a topological insulator, although we have checked that Ca_3PbO is not a topological insulator. Note that it is natural for the surface bands to have no Kramers degeneracy (if we look at one surface), since the spin–orbit coupling is included

in our model and the existence of a surface breaks the inversion symmetry.

The surface band structure for 111 surface is shown in Fig. 9(a). Again, we can see the surface states in Fig. 9(a). As in the case of the 001 surface, the surface bands are nondegenerate if we look at one of the top or bottom surface. These results suggest that the nondegenerate surface states in this model are rather robust, although this system is not a topological insulator. It is a very interesting future problem to clarify the relation between the topological insulators and Ca_3PbO series.

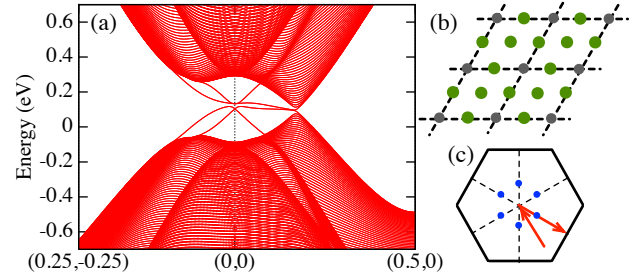


Fig. 9. (Color online) (a) Surface band structure for the 111 surface. (b) Schematic picture for the 111 surface. (c) Surface Brillouin zone for the 111 surface. Dots and arrows represent the same things as in Fig. 8.

6. Summary and Discussion

In this paper, we first constructed a tight-binding model that describes the low-energy band structure of Ca_3PbO . The three Pb- p orbitals and three Ca- $d_{x^2-y^2}$ orbitals are included in the basis set, reflecting the result of the analysis of the orbital weight distributions on the bands. The appropriate choices of the hopping integrals lead to the satisfactory agreement between the band structure obtained in the first-principles calculation and that of the constructed tight-binding model. Especially, the Dirac electrons, which is the most important feature of the band structure of Ca_3PbO , emerge in the tight-binding model.

It was then confirmed that the low-energy effective Hamiltonian in the vicinity of the Fermi energy is really a Dirac Hamiltonian by applying the basis transformation and the expansion of the matrix elements with respect to k_{\pm} . In this procedure, four basis wave functions required for the realization of the Dirac Hamiltonian are identified as $|p_{\frac{3}{2}\frac{3}{2}}\rangle$, $|p_{\frac{3}{2}\frac{3}{2}}\rangle$, $|d'_2\uparrow\rangle$, and $|d'_2\downarrow\rangle$. Each basis wave function corresponds to each components of the pseudospin of the Dirac electron. Therefore the information of the basis wave functions clarified in this paper will play important roles in considering the possible scheme for controlling the internal degrees of freedom of the emergent Dirac electrons.

We have also made a detailed argument on the origin of the mass term of the Dirac electron. The conclusion is that the orbitals other than Pb- p and Ca- $d_{x^2-y^2}$ orbitals and the spin–orbit coupling play key roles in providing the mass term. From this analysis, we can easily understand the reason for the smallness of the mass term.

Namely, the finite mass term requires the inclusion of the orbitals whose weights are lying far away from the Fermi energy. Since the spin-orbit coupling on the Pb atom is essential for the mass term, the mass term can be controlled by replacing Pb atoms by, for example, Sn. Specifically, the alloy of $\text{Ca}_3(\text{Pb}_{1-x}\text{Sn}_x)\text{O}$ will give a smaller mass gap since the spin-orbit coupling of Sn is weaker than that of Pb. In fact, the first-principles calculation for Ca_3SnO results in the smaller mass gap compared with that obtained in Ca_3PbO .¹²

Finally, we have discussed the surface band structures of Ca_3PbO using the constructed tight-binding model. It is found that there exist nontrivial surface bands that cannot be explained as the bulk states projected on the surface Brillouin zone. Note that ref. 11 shows that there should be nontrivial surface states for materials having Weyl fermions. Interestingly, the observed surface states are nondegenerate if we look at one surface. Further studies on the surface band structure in the present model, such as to investigate the relation between Ca_3PbO and topological insulators, are highly desired. In this paper surfaces were treated as simple open boundaries. When we compare the present results and some future experimental results, it will be required to consider the effect of surface potential since the surfaces in Figs. 8(c), 8(d), and 9(b) are not charge neutral.

The successful construction of the simple tight-binding model for Ca_3PbO encourages further search for new materials having Dirac electrons. The detailed analysis provided in this paper are useful in the future experimental and theoretical studies of the Ca_3PbO and related materials.

T.K. was supported by JSPS Research Fellowship.

-
- 1) P. R. Wallace: Phys. Rev. **71** (1947) 622.
 - 2) K. S. Novoselov, A. K. Geim, S. V. Morozov, D. Jiang, M. I. Katsnelson, I. V. Grigorieva, S. V. Dubonos, and A. A. Firsov: Nature **438** (2005) 197.
 - 3) A. H. Castro Neto, F. Guinea, N. M. R. Peres, K. S. Novoselov, and A. K. Geim: Rev. Mod. Phys. **81** (2009) 109.
 - 4) P. Wolff: J. Phys. Chem. Solids **25** (1964) 1057.
 - 5) S. Katayama, A. Kobayashi, and Y. Suzumura: J. Phys. Soc. Jpn. **75** (2006) 054705.
 - 6) N. Tajima and K. Kajita: Sci. Technol. Adv. Mater. **10** (2009) 024308.
 - 7) M. Z. Hasan and C. L. Kane: Rev. Mod. Phys. **82** (2010) 3045.
 - 8) J. K. Wang, L. L. Zhao, Q. Yin, G. Kotliar, M. S. Kim, M. C. Aronson, and E. Morosan: Phys. Rev. B **84** (2011) 064428.
 - 9) J. Park, G. Lee, F. Wolff-Fabris, Y. Y. Koh, M. J. Eom, Y. K. Kim, M. A. Farhan, Y. J. Jo, C. Kim, J. H. Shim, and J. S. Kim: Phys. Rev. Lett. **107** (2011) 126402.
 - 10) K. Wang, D. Graf, H. Lei, S. W. Tozer, and C. Petrovic: Phys. Rev. B **84** (2011) 220401.
 - 11) X. Wan, A. M. Turner, A. Vishwanath, and S. Y. Savrasov: Phys. Rev. B **83** (2011) 205101.
 - 12) T. Kariyado and M. Ogata: J. Phys. Soc. Jpn. **80** (2011) 083704.
 - 13) X. Gonze, J.-P. Michenaud, and J.-P. Vigneron: Phys. Rev. B **41** (1990) 11827.
 - 14) Y. Liu and R. E. Allen: Phys. Rev. B **52** (1995) 1566.
 - 15) L. Wehrli: Z. Phys. B **8** (1968) 87.
 - 16) A. Abrikosov: J. Low Temp. Phys. **8** (1972) 315.
 - 17) J. W. McClure: J. Low Temp. Phys. **25** (1976) 527.
 - 18) P. Blaha, K. Schwarz, G. K. H. Madsen, D. Kvasnicka, and J. Luitz: WIEN2k, An Augmented Plane Wave + Local Orbitals Program for Calculating Crystal Properties (Karlheinz Schwarz, Techn. Universität Wien, Austria), 2001. ISBN 3-9501031-1-2 .
 - 19) A. Widera and H. Schäfer: Mater. Res. Bull. **15** (1980) 1805.
 - 20) J. P. Perdew, K. Burke, and M. Ernzerhof: Phys. Rev. Lett. **77** (1996) 3865.
 - 21) A. H. MacDonald, W. E. Pickett, and D. D. Koelling: J. Phys. C **13** (1980) 2675.
 - 22) K. Haddadi, A. Bouhemadou, L. Louail, and S. Bin-Omran: Solid State Commun. **150** (2010) 1995.
 - 23) D. Cherrad, M. Maouche, M. Maamache, and L. Krache: Physica B **406** (2011) 2714.
 - 24) P. Giannozzi, S. Baroni, N. Bonini, M. Calandra, R. Car, C. Cavazzoni, D. Ceresoli, G. L. Chiarotti, M. Cococcioni, I. Dabo, A. Dal Corso, S. de Gironcoli, S. Fabris, G. Fratesi, R. Gebauer, U. Gerstmann, C. Gougoussis, A. Kokalj, M. Lazzeri, L. Martin-Samos, N. Marzari, F. Mauri, R. Mazzarello, S. Paolini, A. Pasquarello, L. Paulatto, C. Sbraccia, S. Scandolo, G. Sclauzero, A. P. Seitsonen, A. Smogunov, P. Umari, and R. M. Wentzcovitch: J. Phys.: Condens. Matter **21** (2009) 395502.
 - 25) I. Souza, N. Marzari, and D. Vanderbilt: Phys. Rev. B **65** (2001) 035109.
 - 26) A. A. Mostofi, J. R. Yates, Y.-S. Lee, I. Souza, D. Vanderbilt, and N. Marzari: Comput. Phys. Commun. **178** (2008) 685 .
 - 27) J. Kuneš, R. Arita, P. Wissgott, A. Toschi, H. Ikeda, and K. Held: Comput. Phys. Commun. **181** (2010) 1888 .
 - 28) C. Herring: Phys. Rev. **52** (1937) 365.
 - 29) G. F. Koster, J. O. Dimmock, R. G. Wheeler, and H. Statz: *Properties of the Thirty-Two Point Groups* (The M.I.T Press, Cambridge, 1963).
 - 30) L. Fu and C. L. Kane: Phys. Rev. B **76** (2007) 045302.
 - 31) M. König, H. Buhmann, L. W. Molenkamp, T. Hughes, C.-X. Liu, X.-L. Qi, and S.-C. Zhang: J. Phys. Soc. Jpn. **77** (2008) 031007.
 - 32) M. Klintonberg: arXiv:1007.4838.